Article

Nonlinear finite element analysis of ultra-high-performance fiber-reinforced concrete beams

**Doo-Yeol Yoo[1], Su-Tae Kang[2], Nemkumar Banthia[1]
and Young-Soo Yoon[3]**

Abstract

A nonlinear finite element analysis was performed to simulate the flexural behaviors of ultra-high-performance fiber-reinforced concrete beams. For this, two different tension-softening curves obtained from micromechanics-based analysis and inverse analysis were incorporated. For micromechanics-based analysis, two-dimensional and three-dimensional random fiber orientations were assumed to obtain the fiber-bridging curve, and a softening curve of matrix in ultra-high-performance fiber-reinforced concrete was used. The use of tension-softening curves obtained from inverse analysis and micromechanics-based analysis using two-dimensional random fiber orientation exhibited fairly good agreement with the experimental results, whereas the use of tension-softening curve from micromechanics-based analysis using three-dimensional random fiber orientation underestimated the experimental results.

Keywords

Ultra-high-performance fiber-reinforced concrete, finite element analysis, tension-softening curve, micromechanics, fiber orientation

Introduction

Recently, the strength of concrete has been substantially improved by technological advancements. However, since an improvement in concrete strength is inevitably accompanied by brittleness, its application to civil infrastructures is restricted. The incorporation of fibers into the concrete mixture can reduce this brittleness by improving the ductility and energy absorption capacity (Banthia and Nandakumar, 2003). In particular, the ultra-high-performance fiber-reinforced concrete (UHPFRC)

[1]Department of Civil Engineering, The University of British Columbia, Vancouver, BC, Canada
[2]Department of Civil Engineering, Daegu University, Gyeong-buk, Republic of Korea
[3]School of Civil, Environmental and Architectural Engineering, Korea University, Seoul, Republic of Korea

Corresponding author:
Young-Soo Yoon, School of Civil, Environmental and Architectural Engineering, Korea University, Anam-dong 5-ga, Seongbuk-gu, Seoul 136-713, Republic of Korea.
Email: ysyoon@korea.ac.kr

that was recently developed can be a solution for the brittle failure since it provides both superb strength and ductility and is also characterized by strain-hardening with multiple cracks in tension (Wille and Naaman, 2013; Yoo et al., 2013a). However, although UHPFRC exhibits such excellent properties, its application is still limited because of the high cost and a lack of prediction and design technologies.

One of the biggest differences of the design using UHPFRC with that using conventional concrete is to take into account the contribution of fiber bridging to the post-cracking tensile response. For this, fracture mechanics-based inverse analysis has been adopted by many researchers and design codes (AFGC/SETRA, 2002; JSCE, 2004; Uchida et al., 2005; Wille et al., 2014; Yoo et al., 2013b, 2014, 2015a) to provide tension-softening curve (TSC), which is the most important information for determining tensile stress block. Yoo et al. (2014) proposed a generalized TSC of UHPFRC regardless of the fiber length and placement method leading to different fiber orientation distributions by performing numbers of experiments, numerical simulations, and image analyses. Wille et al. (2014) also carried out image analysis to investigate the effect of shape function along the beam height, determined by the fiber orientation and dispersion, on the backward (inverse) analysis and reported that the fiber orientation and distribution over the beam height can be neglected in inverse analysis for determining tensile response. Uchida et al. (2005) introduced a bi-linear TSC obtained from inverse analysis and direct tension test and an equivalent specific length required to transform the crack width to the strain. In addition, Yoo et al. (2015a) successfully predicted the impact response of structural UHPFRC beams from sectional analysis incorporating tri-linear TSC obtained by inverse analysis and single-degree-of-freedom system. Likewise, the material and structural behaviors of UHPFRC have been quite accurately predicted by using TSCs derived from inverse analysis. However, the inverse analysis method requires very complicated programming work, and thus, suggesting a simpler and fundamental method for obtaining appropriate TSC of UHPFRC remains a pressing need.

The improved ductility and energy absorption capacity of UHPFRC can be achieved through fiber bridging at cracked planes. The typical post-cracking tensile responses of pure concrete (or matrix) and fiber-reinforced concrete (FRC) like UHPFRC are illustrated in Figure 1. As indicated in the figure, the stress in concrete or matrix steeply decreases immediately after
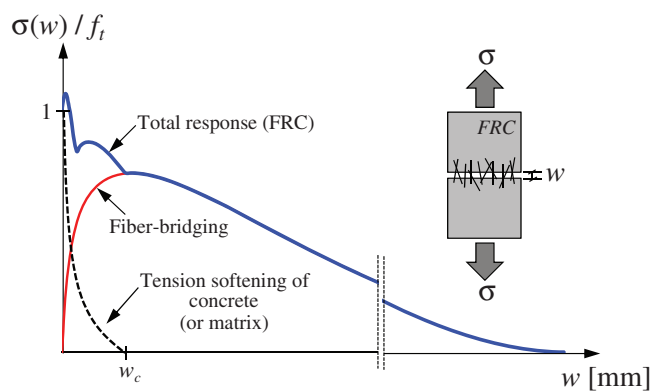

Figure 1. Conceptual post-cracking tensile behavior of FRC (i.e. UHPFRC).

cracking, while the stress in FRC very gradually decreases as a result of the contribution of fibers across cracked surfaces. Thus, the post-cracking tensile behavior of FRC is composed of the contributions of concrete (or matrix) softening and fiber bridging. Therefore, an accurate prediction of the tensile behavior of this material is only possible using a realistic evaluation of the bridging behavior attained with fibers and the softening behavior in concrete (or matrix).

Previously, a method to obtain a fiber-bridging curve of the engineered cementitious composites (ECC) was suggested based on micromechanical approach (Li et al., 1991). Based on this approach, the post-cracking tensile behavior of ECC can be reasonably simulated. This approach is quite rational because regardless of the fiber properties such as the fiber contents and types, the fiber-bridging curve can be predicted using little fundamental information (i.e. fiber pullout load-slip relation, fiber volume content, fiber orientation, etc.). Thus, this can be one of the solutions to overcome the difficulties of inverse analysis and the deficiency in prediction and design technologies for UHPFRC. Unfortunately, however, a lack of research has been conducted on the application of the micromechanics-based approach to UHPFRC (Kang and Kim, 2011) thus far.

Accordingly, in this study, the flexural behaviors of UHPFRC beams with various fiber volume contents were predicted based on the micromechanics-based concept. First, the micromechanics-based fiber-bridging curves were derived with the assumptions of two-dimensional (2D) and three-dimensional (3D) random fiber orientations. Then, the obtained fiber-bridging curves were incorporated into finite element models along with the previously suggested matrix softening curve using user-supplied subroutines and a finite element analysis was conducted. Finally, the analytical predictions were verified through a comparison with the previous test data.

Research significance

Owing to the excellent mechanical and durability properties of UHPFRC, the potential in various applications has attracted interest from researchers. In contrast to conventional concrete, the contribution of fiber reinforcement to the post-cracking tensile response needs to be considered for structural design, and mostly fracture mechanics-based inverse analysis has been applied for the TSC of UHPFRC. However, the inverse analysis method cannot take into account the diversity of fiber orientation distribution and requires very complicated programming work. Thus, the present study proposed an alternative method to provide suitable TSC based on the micromechanics-based concept and conducted numerical analysis by incorporating the suggested TSC to verify the method.

Theoretical approach for TSC

Pre-cracking behavior

Before any cracking is initiated, the external tensile load applied to an FRC consisting of a low modulus matrix with high modulus fibers is transferred from the matrix to the fiber by a shear transfer mechanism (Bentur and Mindess, 2007). Thus, some of the load will be carried by the fibers and the rest by the matrix, and a schematic description of the deformation around the fiber before and after loading is shown in Figure 2(a). The interaction between the matrix and the fiber is generally elastic in nature before cracking. In addition, the shear stress distribution along the embedment length of the fiber is non-uniform, as shown in Figure 2(b). The analytical model for this nonlinear shear transfer, which is the main mechanism of the pre-cracking behavior of an FRC,
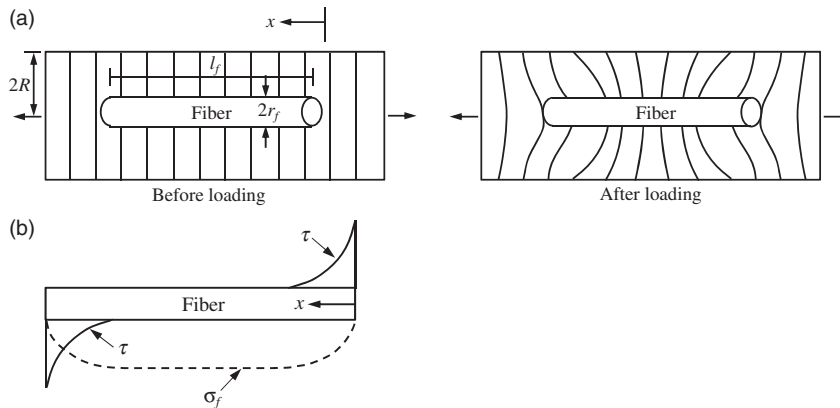
Figure 2. Schematic description of a fiber embedded in matrix, and the deformation and stress fields around it; (a) geometry of the fiber and the deformation in the matrix around the fiber before and after loading, (b) elastic shear stress distribution at the interface and tensile stress distribution in the fiber (Bentur and Mindess, 2007).

was firstly suggested by Cox (1952). According to his model, the tensile stress $\sigma_f(x)$ in the fiber and elastic shear stress at the interface $\tau(x)$ at a distance of x from the fiber end can be calculated by

$$\sigma_f(x) = E_f \varepsilon_m \left\{ \frac{1 - \cosh \beta_1 \left(\frac{l_f}{2} - x\right)}{\cosh \frac{\beta_1 l_f}{2}} \right\} \tag{1}$$

$$\tau(x) = E_f \varepsilon_m \left\{ \frac{G_m}{2E_f \ln(R_m/r_f)} \right\}^{1/2} \frac{\sinh \beta_1 \left(\frac{l_f}{2} - x\right)}{\cosh \frac{\beta_1 l_f}{2}} \tag{2}$$

where

$$\beta_1 = \left\{ \frac{2G_m}{E_f r_f^2 \ln(R_m/r_f)} \right\}^{1/2} \tag{3}$$

Here, the R_m/r_f depends on the fiber packing and the volume contents of fibers. With the assumptions of long fibers having a circular cross-section, the following equations can be used, as shown in Figure 3 (Piggott, 1980). In this study, the hexagonal packing was assumed to be used in accordance with a previous study (Kang and Kim, 2011).

For square packing (Figure 3(a)):

$$\ln(R_m/r_f) = \frac{1}{2} \ln(\pi/V_f) \tag{4a}$$

For hexagonal packing (Figure 3(b)):

$$\ln(R_m/r_f) = \frac{1}{2} \ln\left[2\pi/(3V_f)^{1/2}\right] \tag{4b}$$
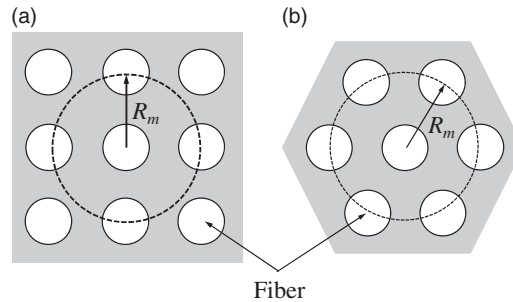
Figure 3. Fiber packing arrangement for R_m in shear lag model; (a) for square packing, (b) for hexagonal packing.

The maximum shear stress at the interface is obtained at both fiber ends and decreases to zero at the center, whereas the tensile stress of the fiber increases from the ends of the fiber inward, and the maximum tensile stress generates at the center (Figure 2(b)).

The tensile stress of the composites can be calculated based on the *rule of mixture*. It is assumed that a uniform strain exists throughout the composite and that failure occurs when either of the materials (matrix or fiber) reaches its failure strain. This can be expressed by

$$\sigma_c(\varepsilon_c) = \sigma_m(\varepsilon_c)V_m + \eta_l\eta_\theta\sigma_f(\varepsilon_c)V_f \tag{5}$$

where

$$\eta_l = 1 - \frac{\tanh(\beta_1 l_f/2)}{(\beta_1 l_f/2)} \tag{6}$$

$$\eta_\theta = \int_{\theta_{\min}}^{\theta_{\max}} p(\theta)\cos^2\theta \mathrm{d}\theta \tag{7}$$

It is possible to obtain fiber orientation coefficient η_θ values of 0.5 for a 2D random orientation and 1/3 for a 3D random orientation. Equation (7) was derived based on the assumption that no enhancement of the tensile strength is achieved when the fibers are aligned perpendicular to the tensile direction, and that the tensile strength is maximized when fibers are aligned parallel to the tensile direction. Thus, $\eta_\theta = 1$ implies that all the fibers are aligned parallel to the tensile direction, and conversely, $\eta_\theta = 0$ indicates that all the fibers are aligned perpendicular to the tensile direction.

The pre-cracking tensile behavior in the composites is influenced by many factors. Among others, the effects of the fiber volume fraction and fiber orientation on the tensile stress–strain relationships were investigated, as shown in Figure 4. In this study, the tensile strain at cracking was assumed to be 236 $\mu\varepsilon$ based on the previous direct tensile test results for UHPFRC (Kang and Kim, 2011). As can be seen, the pre-cracking tensile strength increased with better fiber orientation (2D random fiber orientation) and higher fiber volume fraction, but the increase was insignificant. For example, the first cracking strength for a fiber content of 4% by volume with 2D random fiber orientation was found to be approximately 11.1 MPa, which is just 3.3% higher than that for 1% by volume. By considering the fact that the post-cracking tensile or flexural strength is substantially increased by
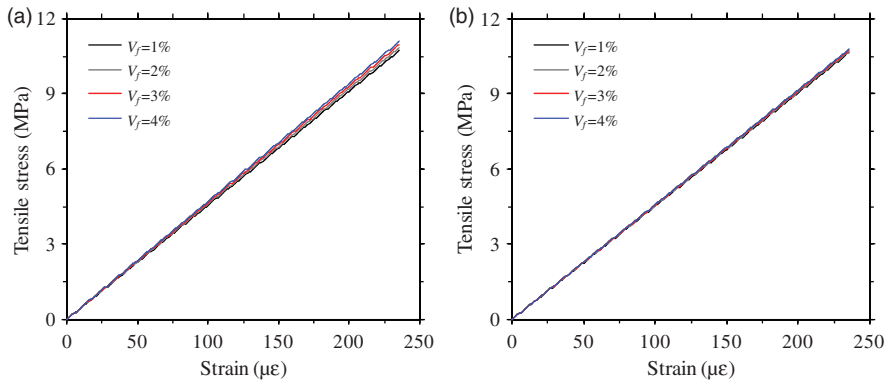
Figure 4. Pre-cracking tensile response of UHPFRC according to fiber orientation; (a) 2D random fiber arrangement, (b) 3D random fiber arrangement.

the fiber content and influenced by the fiber orientation (Yoo et al., 2013b, 2014), it can be said that the effects of the fiber volume content and fiber orientation on the first cracking strength are relatively negligible. This is because the first cracking strength is more affected by the matrix strength, rather than the fiber-bridging effect.

Post-cracking behavior

Modeling pullout behavior of single fiber. The post-cracking tensile behavior of FRC is mainly influenced by the fiber characteristics, rather than the matrix characteristics. This is because with increasing crack width, the tensile load between the crack surfaces is mostly resisted by the fibers. Therefore, to analyze the post-cracking behavior of FRC, the pullout behavior of a single fiber should be determined.

The pullout behavior of a steel fiber embedded in a cementitious matrix is divided into three categories: (a) perfect bonding region, (b) partial debonding region, and (c) full debonding region. Here, categories (a) and (b) are included in the ascending branch, while the category (c) is included in the descending branch. Lee et al. (2010) suggested an analytical model for predicting the pullout load-slip response of a smooth steel fiber embedded in an ultra-high-strength cementitious matrix having the properties almost identical to those used in this study. In their study, the modeling of the ascending branch was derived based on the ideas from Naaman et al. (1991), with the only difference being the assumption that the frictional shear stress is identical to the bond strength. The relationship between bond shear stress and slip is characterized by a linear-elastic up to the point of bond strength and a constant frictional shear stress beyond the bond strength. On the basis of this relationship, the pullout behavior of aligned fiber, defined by the relation of force and displacement at the free end of fiber, was suggested in terms of using free-body diagram of infinitesimal segment of fiber and static equilibrium condition that the external force is equal to the summation of local forces in the fiber and matrix. To consider the fiber orientation effect on the bond strength and the corresponding slip, they also used the apparent bond strength and slip concepts. The modeling of the descending branch was derived by assuming that the frictional shear stress with a larger slip was decayed. In Naaman's approach, the decay of the frictional stress was considered by using an exponential function for the deterioration of a fiber-matrix misfit (an asymptotic decaying
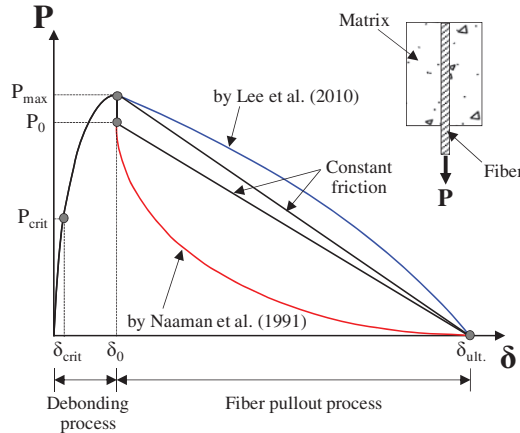
Figure 5. Pullout behaviors of single smooth steel fiber embedded in cementitious matrix.

model), as illustrated in Figure 5. However, Lee et al. (2010) reported that the pullout behavior of a smooth steel fiber embedded in an ultra-high-strength matrix was completely different from an asymptotic decaying model. Thus, they suggested a new fictional slip model that is applicable to an ultra-high-strength matrix (Figure 5). The major reason why ultra-high-strength matrix provides much better pullout resistance in the full debonding region than previous normal- and high-strength matrices was that the accumulation of abraded particles of matrix toward the fiber pullout end, which leads to a wedge effect, causes a high frictional bond (Wille and Naaman, 2013). Thus, the pullout load and slip relations of a single fiber with the inclination angle can be expressed by the following equations. The detailed derivation of the equations is provided elsewhere (Lee et al., 2010; Yoo, 2014).

a. a perfect bonding region in the ascending branch (before the critical pullout load when the shear stress acting on the fiber and matrix at $x = l$ reaches its bond strength ($P \leq P_{crit}$)):
   The fiber presents a perfect bond with the matrix, and in this case, the pullout load-slip behavior is linear and can be expressed as follows.

$$\left(\frac{P}{\delta}\right)(\theta) = \frac{1/2}{1 + \gamma\left(\frac{2\theta}{\pi}\right)^n} \frac{\lambda A_m E_m}{Q - 2} \frac{1 + e^{-\lambda l}}{1 - e^{-\lambda l}} \tag{8}$$

b. a partial debonding region in the ascending branch (after the critical pullout load when the shear stress acting on the fiber and matrix at $x = l$ reaches its bond strength ($P > P_{crit}$) and before the complete debonding of the interface):
   The fiber is partially debonded from the matrix, while the remaining part is still fully bonded to the matrix. Thus, the load P is resisted by the resistance of the fiber in both the bonded and debonded zones, and the pullout response is expressed as follows.

$$P(\theta) = \pi d_f \tau_{f(\text{app})}(\theta)u + \frac{\pi d_f \tau_{\max(\text{app})}(\theta)}{\lambda} \frac{1 - e^{-2\lambda(l-u)}}{\frac{2}{Q}e^{-\lambda(l-u)} + \left(1 - \frac{1}{Q}\right)\left[1 + e^{-2\lambda(l-u)}\right]} \tag{9}$$

$$\delta(\theta) = \left[1 + \gamma\left(\frac{2\theta}{\pi}\right)^n\right]\frac{2}{A_m E_m}\left\{P(\theta)(Q-1)u - \frac{\pi d_f \tau_{f(\mathrm{app})}(\theta)u^2}{2}(Q-2)\right.$$
$$\left. + \left(P(\theta) - \pi d_f \tau_{f(\mathrm{app})}(\theta)u\right)\left[\frac{1 - e^{-\lambda(l-u)}}{1 + e^{-\lambda(l-u)}}\right]\frac{Q-2}{\lambda} - \pi d_f \tau_{f(\mathrm{app})}(\theta)ul\right\} \tag{10}$$

c. a full debonding region in the descending branch (after the complete debonding of the interface):

Once complete debonding occurrs at the fiber and matrix interface, the fiber acts as a rigid body, and the relative displacement due to the elastic elongation of the fiber is neglected. Therefore, the pullout response can be expressed by the following equations.

$$x = \left(l^2 - \delta l\right)/(l - 2\delta_0) \tag{11}$$

$$P = \pi d_f \tau_{fd}(\delta)x \tag{12}$$

$$\tau_{fd}(\delta) = \tau_{f(\mathrm{app})}(\theta)\exp[-\eta(\delta - 2\delta_0)^\alpha]\frac{\left(1 - \exp\left\{\frac{-2v_f\mu x}{E_f r_f\left[\frac{(1+v_m)}{E_m} + \frac{(1-v_f)}{E_f}\right]}\right\}\right)}{\left(1 - \exp\left\{\frac{-2v_f\mu l}{E_f r_f\left[\frac{(1+v_m)}{E_m} + \frac{(1-v_f)}{E_f}\right]}\right\}\right)} \tag{13}$$

Based on the image analysis for UHPFRC with 2% by volume of steel fibers ($l_f/d_f = 13/0.2$ mm/mm) (Yoo et al., 2014), the number of fiber per unit area was found to be 0.340 and 0.399 number/mm^2, respectively. Thus, the ratios of fiber area and area of matrix (A_f/A_m) were obtained by approximately 0.010 and 0.013, respectively, and thus, the areas of matrix affected by the single fiber were approximately 100 and 80 times larger than the area of fiber. Since a higher value of A_m/A_f less influences on the analytical results (Kang, 2010), the ratio A_m/A_f of 100 was conservatively adopted in this study. In addition, the elastic modulus of matrix (E_m) was adopted by 45 GPa, and the Poisson's ratios of the fiber (v_f) and the matrix (v_m) were applied by 0.3 and 0.2, respectively. The coefficients η, reflecting steepness of descending branch in fiber pullout curve, and α, determining initial slope of frictional slip behavior, were also adopted by 0.05 and 1, respectively, and the frictional coefficient μ was assumed to be 0.3 (Pallett et al., 2002)

Lee et al. (2010) experimentally verified that the bond strength of smooth steel fibers embedded in ultra-high strength matrix increases with the inclination angle and the largest bond strength is obtained at an angle of 30° or 45°. Li et al. (1990) also reported that the bond strength of synthetic fibers increases when the fibers are inclined in the tensile load direction, as a result of the local interaction forces (matrix reaction force R and friction force μR) between the fiber and the matrix at the exit point, as illustrated in Figure 6. This phenomenon is called the *snubbing effect*. In addition, a local failure of matrix occurs at the matrix wedge as a result of the stress concentration from the pullout load of the inclined fiber. This is called the *matrix spalling effect*. Matrix spalling leads to a drop of the pullout load, as well as an increase in the crack opening displacement owing to the change of the embedment length. The inclined steel fiber provides the gradual spalling of the matrix, together with the snubbing effect. Thus, the combined effects of the snubbing and matrix spalling should be considered when modeling the pullout behavior of an inclined fiber.
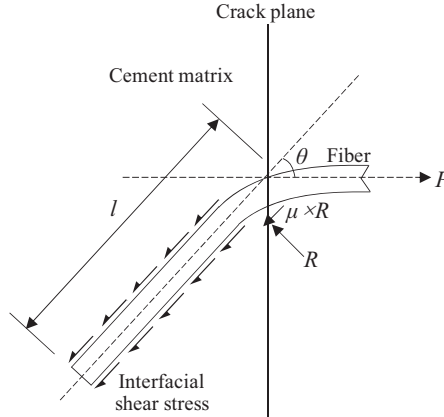
Crack plane

Cement matrix

θ Fiber

P

l

$\mu \times R$

R

Interfacial
shear stress

Figure 6. Schematic description of crack bridging of obliquely aligned fiber (Kanda and Li, 1980).

By considering these effects on the bond behavior, the apparent bond strength and frictional shear stress ($\tau_{\max(app)}$ and $\tau_{f(app)}$) are calculated by

$$\tau_{\max(app)}(\theta) = \tau_{f(app)}(\theta) = e^{f\theta}(\cos\theta)^k \tau(\theta = 0) \tag{14}$$

Lee et al. (2010) proposed the values of 1.6 and 1.8 for the coefficients f (for snubbing effect) and k (for matrix spalling effect), respectively, based on their single fiber pullout test results. Since the materials (smooth steel fibers and ultra-high-strength cementitious matrix) used in this study were very similar to those used in their study, the coefficients f and k of 1.6 and 1.8 were also adopted.

The slip at the peak pullout load also increases with the inclination angle. Thus, the increase in the slip at the peak is reflected by considering coefficient β, as follows

$$\delta(\theta) = \beta\delta(\theta = 0) \tag{15}$$

where

$$\beta = 1 + \gamma\left(\frac{2\theta}{\pi}\right)^n \tag{16}$$

Lee et al. (2010) suggested $\gamma = 100$ and $n = 2$ for the steel fiber embedded in an ultra-high-strength matrix. An identical steel fiber and very similar matrix were used in this study; thus, $\gamma = 100$ and $n = 2$ were also adopted.

The apparent strength of polyvinylalcohol (PVA) fiber decreased with the inclination angle of the fiber. This is because the fiber and matrix interaction at the exit point leads to additional stress by bending. On the other hand, the steel fiber is much stiffer in bending than the PVA fiber, and thus, the degraded fiber strength (apparent fiber strength) was not considered in this study. In addition, the maximum stress in smooth steel fiber embedded in an ultra-high-strength matrix was found to be 981.12 MPa, approximately 39% of tensile strength of fiber (=2500 MPa) (Yoo et al., 2015b), and no fiber fracture was obtained regardless of the fiber inclination angle (Lee et al., 2010). Therefore, it was assumed that all fibers are pulled out without breakage, in contrast to the previous modeling for ECC (Lin et al., 1999).
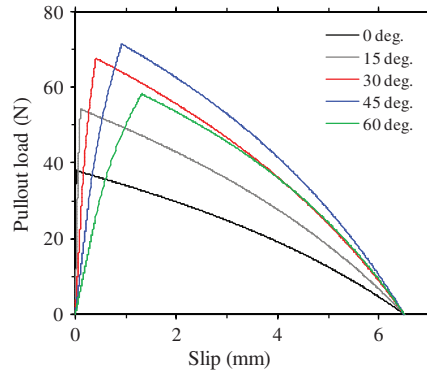
Figure 7. Analytical pullout behaviors of single steel fiber embedded in the matrix with 1% by volume of fibers ($\tau_{max} = 9.31$ MPa).

Several researchers (Markovic, 2006; Yoo et al., 2013b) have mentioned that the bond strength is influenced by the fiber content in the matrix. Thus, in this study, different bond strengths according to the fiber volume content in the matrix were used based on previous pullout test results (Yoo et al., 2013b). It was assumed that the fiber content in the matrix did not affect the coefficients f, k, and β. The typical pullout load and slip response of the steel fiber embedded in the matrix at 1% by volume of fibers, according to the inclination angle, are shown in Figure 7. The variation in the maximum pullout load and the corresponding slip, depending on the inclination angle, was well reflected by using the above equations.

Modeling fiber-bridging curve by multiple fibers. In the case of 2D or 3D, the number of fibers in a unit area is affected by the fiber orientation and embedment length. Figure 8 shows a fiber arbitrarily located at a distance of z from the matrix crack plane to the centroid of the fiber and with an inclination angle of θ to the tensile load direction. Therefore, the embedment length can be expressed by (Li et al., 1991)

$$l = \frac{l_f}{2} - \frac{z}{\cos \theta} \tag{17}$$

For a uniform random distribution, the probability density function of z is $p(z) = 2/l_f$. Thus, by using the probability density functions for θ and z, where the variable z is replaced by l, the number of fibers in a unit area can be given by

$$N_b = \frac{4V_f}{\pi d_f^2} \int_0^{\pi/2} \int_0^{l_f/2} p(l)\, p(\theta) \cos \theta \, \mathrm{d}l \, \mathrm{d}\theta \tag{18}$$

The resistance force of a single fiber at the crack plane is given as a function of the inclination angle θ, embedment length l, and amount of slip δ, which is denoted by $P(\theta, l, \delta)$. Thus, the fiber-bridging stress in the composites can be calculated by

$$\sigma_b(\delta) = \frac{4V_f}{\pi d_f^2} \int_0^{\pi/2} \int_0^{l_f/2} P(\theta, l, \delta)\, p(l)\, p(\theta) \cos \theta \, \mathrm{d}l \, \mathrm{d}\theta \tag{19}$$
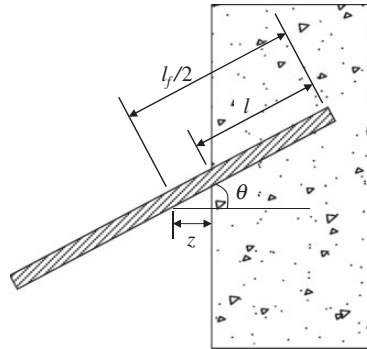
Figure 8. Embedment length of fiber with inclination angle.
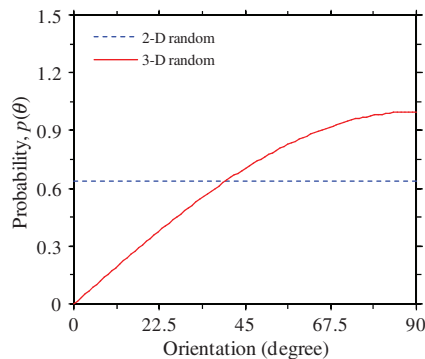

Figure 9. Probability density function for 2D and 3D random fiber orientations.

As shown in the above equations, the fiber-bridging stress varies with the fiber orientation. Thus, two different fiber orientations (2D and 3D random fiber orientations) were considered in this study. For the 2D random fiber orientation, $p(\theta)$ was $2/\pi$, while for the 3D random fiber orientation, $p(\theta)$ was given by $\sin\theta$, as given in Figure 9 (Li et al., 1991).

Figure 10 shows the calculated fiber-bridging curves of UHPFRC with four different fiber volume fractions for 2D and 3D random fiber orientations. As indicated in the figure, the fiber-bridging strength increased with an increase in the fiber content as a result of the increase in the number of fibers. In addition, regardless of the fiber content, the 2D random fiber orientation exhibited the higher fiber-bridging stress than the 3D random fiber orientation. This was caused by the higher number of fibers at the crack plane produced by the better fiber orientation obtained with the 2D random fiber orientation compared to that of the 3D random fiber orientation. For example, in the case of the specimen with $V_f = 2\%$, the calculated number of fibers in a unit area was found to be 0.4043 (number/mm^2) for the 2D random fiber orientation and 0.3155 (number/mm^2) for the 3D random fiber orientation.

Matrix softening curve. The post-cracking behavior of FRC is defined by the combined behaviors of concrete (or matrix) softening and fiber bridging. Thus, both the fiber-bridging curve and the softening curve for the concrete should be determined. To date, numerous softening models (i.e.
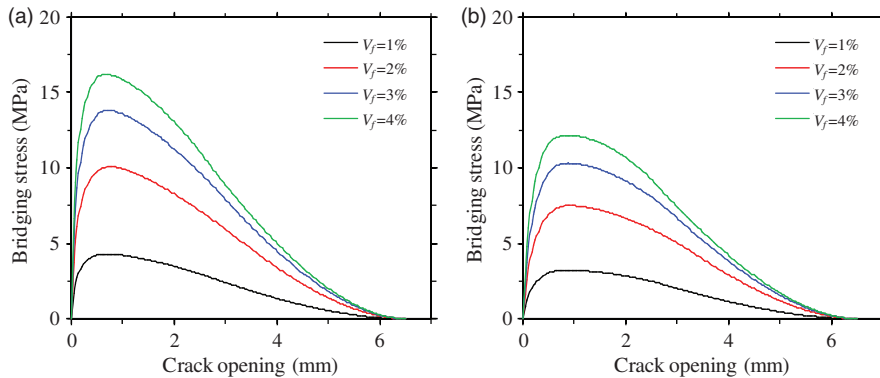
Figure 10. Fiber bridging behaviors of UHPFRC according to fiber content; (a) 2D random fiber orientation, (b) 3D random fiber orientation.
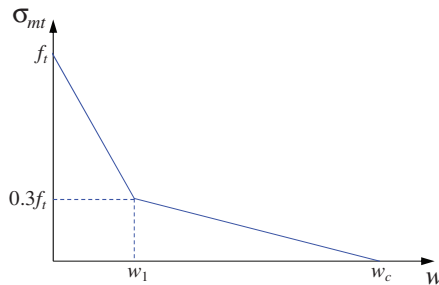

Figure 11. Bilinear softening model of UHPFRC matrix (Kang and Kim, 2011).

linear, bilinear, and exponential curves) have been developed for concrete. However, in the case of UHPFRC, very fine aggregate and high volume fraction of fibers were included without any coarse aggregate. Thus, the UHPFRC matrix showed a different softening behavior with that of previous concrete. Yet, unfortunately, there is no published study on the tension-softening model for this matrix. Kang and Kim (2011) attempted to predict the tensile behavior of UHPFRC using the softening curve of concrete calculated by the CEB-FIP Model Code 1990 (CEB, 1993) with the assumption of that a very small size of coarse aggregate was used. However, the analytical prediction showed a narrow crack opening range, and the behavior appeared to be different from that of an ultra-high-strength matrix with fibers, which is much more ductile than the calculated softening curve. For this reason, they suggested a new bilinear model for the softening curve of an ultra-high-strength matrix with fibers, as expressed by (see Figure 11)

$$\sigma_{mt} = f_t\left[1 - 0.7\frac{w}{w_1}\right] \quad \text{for } 0.3f_t \leq \sigma_{mt} \leq f_t \tag{20}$$

$$\sigma_{mt} = \frac{0.3f_t}{w_c - w_1}(w_c - w) \quad \text{for } 0 \leq \sigma_{mt} \leq 0.3f_t \tag{21}$$

Table 1. Mix proportions.

	Relative weight ratios to cement						Steel fiber (V_f, %)	Flow (mm)
	Cement	Water	Silica fume	Sand	Silica flour	Superplasticizer		
$V_f=1\%$	0.2	1	0.25	0.30	1.10	0.012	1%	235
$V_f=2\%$						0.012	2%	230
$V_f=3\%$						0.014	3%	225
$V_f=4\%$						0.016	4%	210

where V_f = volume fraction of fiber.

Table 2. Properties of smooth steel fiber.

d_f (mm)	l_f (mm)	Aspect ratio (l_f/d_f)	Density (g/cm³)	Tensile strength (MPa)	Elastic modulus (GPa)	Image
0.2	13.0	65.0	7.8	2500	200	

where d_f = diameter of fiber and l_f = length of fiber.

where

$$w_1 = 0.2 \text{ mm} \text{ and } w_c = 0.5 \text{ mm} \tag{22}$$

The cracking tensile strength calculated by using equation (5) (based on the "rule of mixture") at the tensile strain of 236 $\mu\varepsilon$, which was proposed by Kang and Kim (2011), was used as the value of tensile strength f_t in equations (20) and (21).

Experiments

Three-point bending tests of UHPFRC beams with four different fiber volume fractions ($V_f=1\%$, 2%, 3%, and 4%) were carried out in a previous study (Yoo et al., 2013b). The mix proportions used are summarized in Table 1, and the properties of used steel fibers are listed in Table 2. In addition, the detailed geometry of specimen and test setup is shown in Figure 12. Three prismatic specimens for each variable with cross-sectional dimensions of 100 mm × 100 mm and a length of 400 mm were fabricated and tested. A 10-mm-notch was applied at the mid-length of the beam, and a clear span length of 300 mm was used. In order to provide uniform fiber dispersion and alignment, all of the test specimens were fabricated by placing concrete parallel to the longitudinal direction of the specimen, as shown in Figure 13 (Kang et al., 2011). A uniaxial load was applied using a closed-loop, servo-controlled, universal testing machine (UTM) with a maximum load capacity of 250 kN through displacement control. To measure the net deflection of the beams, which excludes the
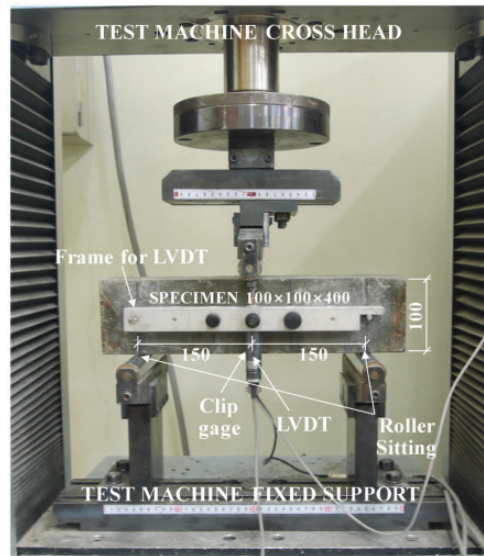
Figure 12. Test setup for three-point bending test.
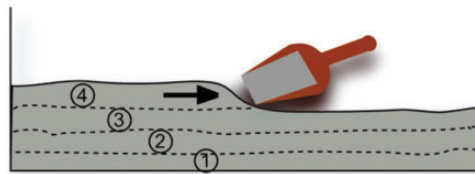

Figure 13. Placement method: placing concrete parallel to the longitudinal direction of beam.

support settlement, a steel frame with linear variable differential transformer (LVDT) was installed at the middle of the beam height on both sides of the specimen (Figure 12). In addition, for measuring crack mouth opening displacement (CMOD), a clip gage with a maximum capacity of 10 mm was attached at the notch of the beam. The applied load, mid-span deflection, and CMOD were measured simultaneously during the testing.

Figure 14 shows the average flexural responses of UHPFRC beams according to the fiber content. Since the individual load–deflection curves exhibited similar shapes each other, the following averaging procedure was used. The deflection was first assumed to increase in 0.01 mm increments, and then, the load was calculated based on a linear interpolation. After that, the load data were averaged at a fixed deflection. This average procedure has been adopted by several researchers for its simplicity (Zhao et al., 2008). When the fiber volume content increased, higher flexural strength and deflection capacity (deflection at the peak) were obtained, whereas a steeper decrease in the flexural load carrying capacity versus deflection was obtained after the peak. On the other hand, the first cracking strength and corresponding deflection and CMOD exhibited no noticeable difference according to the fiber volume fraction. This is caused by the fact that the stress at the first cracking point is mainly determined by the matrix strength rather than the fiber-bridging capacity, as explained above. For example, the highest flexural strength of 45.0 MPa was obtained for the specimen with $V_f = 4\%$, approximately 88.4%, 38.0%, and 9.2% higher than those of the specimens with $V_f = 1\%$, $V_f = 2\%$, and $V_f = 3\%$, respectively. In contrast, the highest first cracking strength of
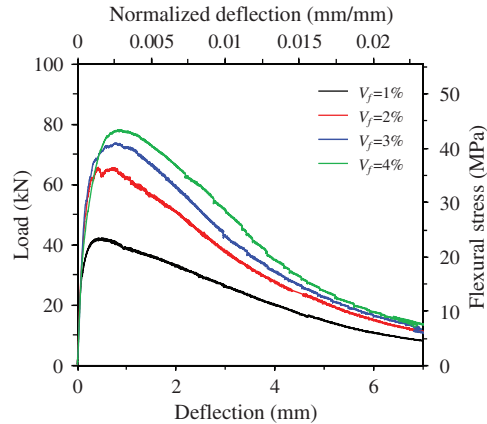
Figure 14. Flexural load versus deflection behaviors (Yoo et al., 2013b).
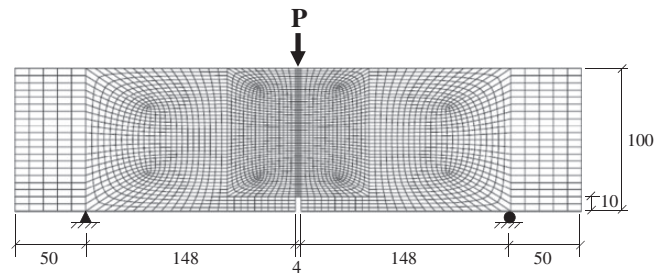

Figure 15. Finite element model for notched beam with center point loading (unit: mm).

12.2 MPa was obtained for the specimen with $V_f = 3\%$, approximately 1.2%, 0.2%, and 2.8% higher than those of the specimens with $V_f = 1\%$, $V_f = 2\%$, and $V_f = 4\%$, respectively. Thus, it was verified that the fibers primarily affects the post-cracking behavior, rather than the pre-cracking behavior of UHPFRC.

Nonlinear finite element analysis

Modeling

To verify the micromechanics-based fiber-bridging curve obtained from two different fiber orientations, a finite element analysis was carried out using the commercial program DIANA (2007). Figure 15 shows the geometry and finite element meshes for UHPFRC beam with 10 mm notch at the center. In order to model the concrete, a four-node quadrilateral isoparametric plane stress element (Q8MEM), which is based on linear interpolation and Gauss integration, was adopted. The total number of elements used was 3584. The discrete crack model, which is useful in situations where the crack pattern can be predicted like a notched beam, was adopted to simulate the crack propagation at the assumed interface element (L8IF) between two lines in a 2D configuration at the

Table 3. Coefficients a and b for ascending branch and parameter w_s for descending branch of fiber bridging curve.

		In equation (23)			In equation (24)
	Fiber orientation	a	b	R^2	w_s (mm)
$V_f=1\%$	2D random	5.750	0.735	0.99707	0.683
	3D random	5.248	0.899	0.99726	0.878
$V_f=2\%$	2D random	5.295	0.738	0.99697	0.748
	3D random	4.709	0.905	0.99685	0.910
$V_f=3\%$	2D random	5.546	0.736	0.99701	0.715
	3D random	5.027	0.903	0.99697	0.878
$V_f=4\%$	2D random	5.910	0.732	0.99697	0.650
	3D random	5.457	0.896	0.99749	0.910

where, R^2=coefficient of determination.

notched center of the beam. Based on previous mechanical test results, UHPFRC exhibited almost linear compressive and tensile behaviors up to cracking (Yoo et al., 2013a, 2015b). Therefore, the pre-cracking behavior at the interface element was assumed to be linear elastic, and the elements outside the assumed crack area were also simply defined to exhibit linear elastic response. In contrast, the post-cracking tensile behavior at the interface element was determined by combining the matrix softening curve and fiber-bridging curve with consideration of fiber orientation.

To incorporate the fiber-bridging curve into finite element modeling using user-supplied subroutines for the post-cracking tensile modeling, a simplified equation for the stress-crack opening relation is required. Therefore, for the ascending branch of the fiber-bridging curve, the following equation was suggested based on the model of Gopalaratnam and Shah (1985), which is for the stress-crack opening relation in the softening curve of concrete.

$$\sigma_b = \sigma_{ub}\left(1 - e^{-aw^b}\right) \tag{23}$$

The coefficients a and b are summarized in Table 3, and Figure 16(a) shows a typical comparison of the ascending branches of the fiber-bridging curves obtained from the micromechanics-based approach and equation (23). The ascending branch of the fiber-bridging curve obtained from the micromechanics-based approach was quite well predicted using equation (23) (i.e. the coefficient of determination (R^2) was found to be over 0.99 for all cases). Thus, it was concluded that this equation is appropriate for modeling the ascending branch in the fiber-bridging curve of UHPFRC.

In the case of the descending branch, a simple linear softening curve suggested by Kang and Kim (2011) was adopted in this study, as equations (24) and (25), and the parameter w_s is given in Table 3.

$$\sigma_b = \frac{4(l_f/2)V_f\tau_f}{\pi d_f}\left(1 - \frac{w - w_s}{0.85(l_f/2) - w_s}\right) \quad \text{for } w \leq 0.85(l_f/2) \tag{24}$$

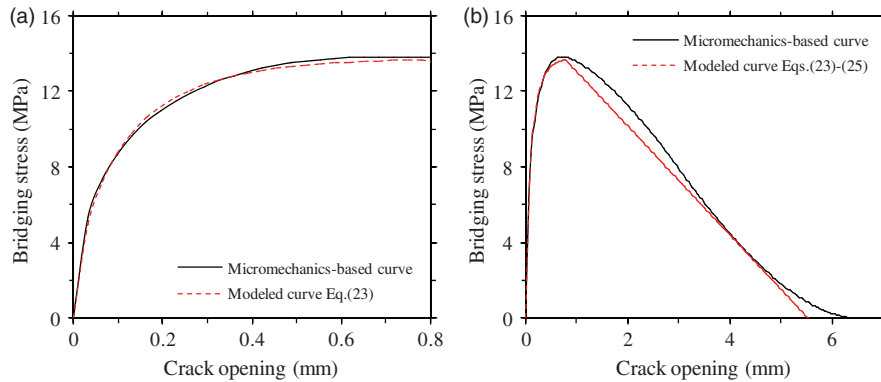$$\sigma_b = 0 \quad \text{for } w > 0.85(l_f/2) \tag{25}$$

Figure 16. Comparison of fiber bridging curves from micromechanics-based modeling and equations (23) to (25); (a) ascending branch, (b) overall bridging curve.
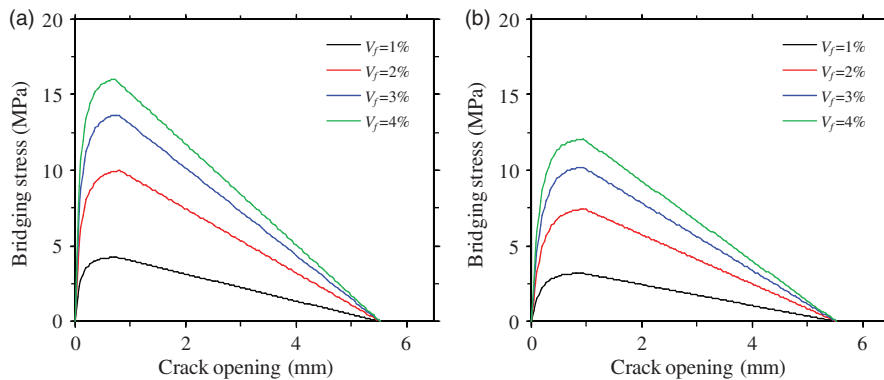

Figure 17. Modeled fiber bridging curves; (a) 2D random fiber orientation, (b) 3D random fiber orientation.

An overall comparison between the micromechanics-based fiber-bridging curve and the modeled fiber-bridging curve is illustrated in Figure 16(b). The modeled fiber-bridging curve calculated by equations (23) to (25) showed good agreement with the bridging curve obtained from the micromechanics-based approach. Thus, the modeled fiber-bridging curves, as shown in Figure 17, were incorporated into the finite element modeling along with the matrix softening curves from equations (20) to (22).

Bilinear TSCs, which have been previously suggested by the authors (Yoo et al., 2013b) based on an inverse analysis, were also considered for comparison. These curves are shown in Figure 18, and detailed information about the parameters in the curves and fracture energy can be found in the previous paper (Yoo et al., 2013b).

Verification

A comparison of the load versus deflection responses of the UHPFRC beams obtained from the experiments and finite element analyses is shown in Figure 19. Naturally, the flexural behaviors of UHPFRC beams including maximum load, deflection capacity, and post-peak softening are fairly
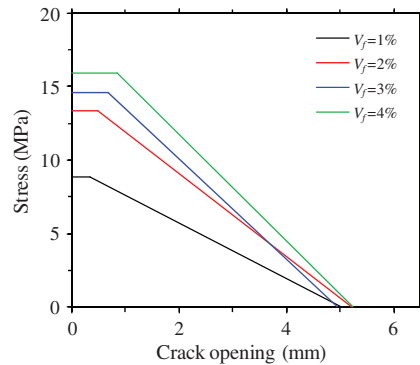
Figure 18. Bilinear tension-softening curves for UHPFRC with various fiber contents (Yoo et al., 2013b).
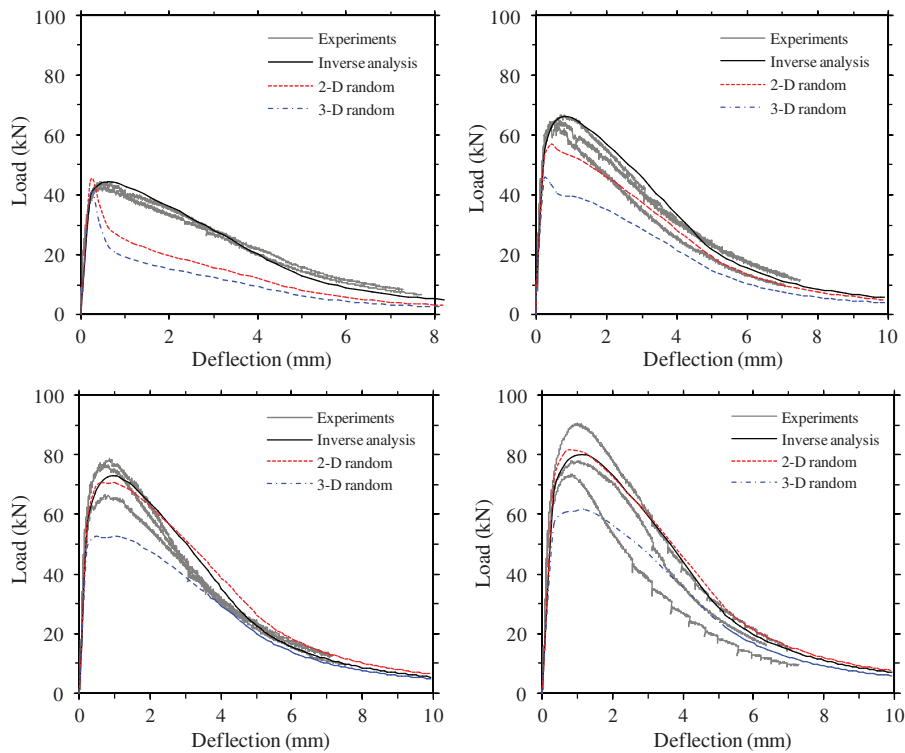

Figure 19. Comparison of experimental and analytical results; (a) $V_f = 1\%$, (b) $V_f = 2\%$, (c) $V_f = 3\%$, (d) $V_f = 4\%$.

well predicted through the finite element analyses using the TSCs from inverse analyses, since the TSCs were inversely derived by the flexural test results. In the case of the micromechanics-based approach, the assumption of a 2D random fiber orientation showed good predictions compared to the experimental results, whereas the assumption of a 3D random fiber orientation resulted in underestimations for the entire test series. For the specimen with $V_f = 1\%$, however, even though the maximum load was well predicted from the micromechanics-based models with both 2D and 3D
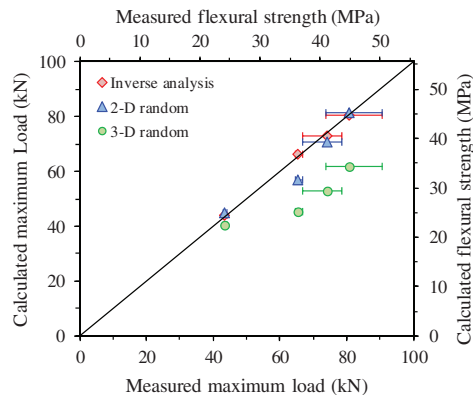
Figure 20. Comparison of maximum bending loads from experiments and analyses.

random fiber orientations, the post-peak softening behaviors seen in the experiments and models were significantly different. This could be mainly due to the discrepancy between the real fiber orientation and the assumptions.

Figure 20 summarizes the comparisons between the measured and predicted maximum loads. Even though some of the specimens exhibited a great degree of scatter, the analytical predictions using the TSCs from both the inverse analysis and the micromechanics-based model with the 2D random fiber orientation showed good agreement with the average values of the measured maximum loads. In contrast, the analyses using the TSCs from the micromechanics-based model with the 3D random fiber orientation underestimated the maximum loads. As shown in Figure 21, the failure mode and deflection shape from the finite element analysis exhibited good agreement with those from the experiment. From these analytical results, it was concluded that the flexural responses of UHPFRC beams can be predicted using a finite element analysis based on the TSCs from both of the inverse analysis and the micromechanics-based model with a 2D random fiber orientation.

Conclusions

In this study, finite element analyses incorporating two different TSCs obtained from inverse analysis and micromechanics-based analysis were performed to predict the flexural responses of UHPFRC beams with various fiber contents. The analytical predictions were verified through comparisons with the previous test data. From the above discussions, the following conclusions can be obtained:

(1) The pre-cracking tensile behavior and first cracking strength were analyzed based on the rule of mixture. The first cracking strength slightly increased with an increase in the fiber content and a better fiber orientation, but this increase was insignificant (the difference between the highest and lowest values was within 3.3%). This is because the first cracking strength is mainly influenced by the matrix strength, rather than the fiber-bridging effect.

(2) To obtain the post-cracking TSC, a micromechanics-based approach for the fiber-bridging curve and the matrix softening curve suggested by Kang and Kim (2011) was adopted in this study. The pullout behaviors of a single fiber embedded in a UHPFRC matrix with various inclination angles were derived based on the model suggested by Lee et al. (2010), and the derived pullout model was extended to the fiber-bridging curve with multiple fibers. To do this, two different (2D
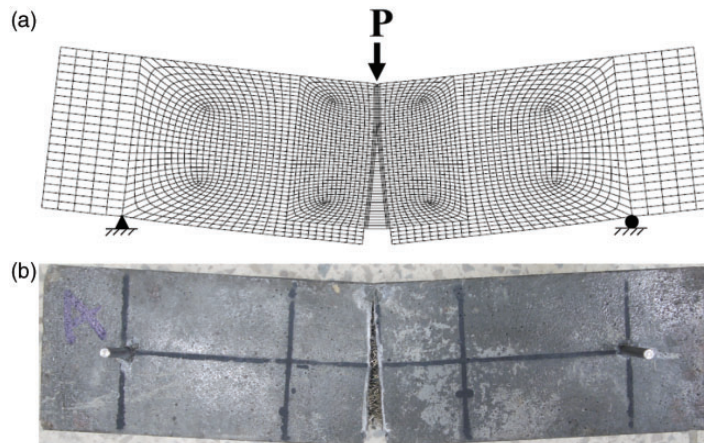
Figure 21. Failure mode and deflection shape; (a) numerical analysis, (b) experiment.

and 3D random) fiber orientations were assumed. The analytical results showed that a higher fiber-bridging strength was obtained by increasing the fiber content and by using the 2D random fiber orientation than the 3D random fiber orientation.

(3) Based on the flexural test results, the load carrying capacity, deflection at the peak, and post-peak ductility were influenced by the fiber content; with an increase in the fiber content, higher load carrying capacity, higher deflection at the peak load, and a steeper decrease in the post-peak load carrying capacity versus deflection were obtained. In contrast, the first cracking strength and the corresponding deflection were insignificantly affected by the fiber content. Thus, it was found that the fibers primarily influence the post-cracking behavior rather than the pre-cracking behavior.

(4) To verify the calculated micromechanics-based TSCs, finite element analyses were carried out, and the analytical results were compared with the test data. In general, the use of the TSCs obtained from the micromechanics-based analysis with the 2D random fiber orientation and from the inverse analysis exhibited fairly good agreement with the experimental results, whereas the use of the TSC obtained from the micromechanics-based analysis with the 3D random fiber orientation underestimated the test results.

Declaration of Conflicting Interests

Funding

References

AFGC/SETRA (2002) *Ultra High Performance Fibre-Reinforced Concretes*. Bagneux, France: Interim Recommendations, SETRA, p. 152.

Banthia N and Nandakumar N (2003) Crack growth resistance hybrid fiber reinforced cement composites. *Cement and Concrete Composites* 25(1): 3–9.

Bentur A and Mindess S (2007) *Fibre Reinforced Cementitious Composites*. 2nd ed. New York: Taylor & Francis.

CEB-FIP (1993) *CEB-FIP Model Code 1990*. London: Thomas Telford.

Cox HX (1952) The elasticity and strength of paper and other fibrous materials. *British Journal of Applied Physics* 3(3): 72–79.

DIANA (2007) *User's Manual – Release 9.2*. Delft, The Netherlands.

Gopalaratnam VS and Shah SP (1985) Softening response of plain concrete in direct tension. *ACI Journal* 82(3): 310–323.

JSCE (2004) *Recommendations for Design and Construction of Ultra-High Strength Fiber Reinforced Concrete Structures (Draft)*. Tokyo, Japan: Japan Society of Civil Engineers.

Kang ST (2010) *Flow-dependent fiber orientation distribution and its effect on the tensile behavior of ultra high performance cementitious composites*. PhD Thesis, Korea Advanced Institute of Science and Technology, Daejeon, Korea, p.243.

Kang ST and Kim JK (2011) The relation between fiber orientation and tensile behavior in an ultra high performance fiber reinforced cementitious composites (UHPFRCC). *Cement and Concrete Research* 41(10): 1001–1014.

Kanda T and Li VC (1980) Interface property and apparent strength of high-strength hydrophilic fiber in cement matrix. *Journal of Materials in Civil Engineering* 10(1): 5–13.

Kang ST, Lee BY, Kim JK, et al. (2011) The effect of fibre distribution characteristics on the flexural strength of steel fibre-reinforced ultra high strength concrete. *Construction and Building Materials* 25(5): 2450–2457.

Lee Y, Kang ST and Kim JK (2010) Pullout behavior of inclined steel fiber in an ultra-high strength cementitious matrix. *Construction and Building Materials* 24(10): 2030–2041.

Li VC, Wang Y and Backer S (1990) Effect of inclining angle, bundling and surface treatment on synthetic fiber pull-out from a cement matrix. *Composites* 21(2): 132–140.

Li VC, Wang S and Backer S (1991) A micromechanical model of tension-softening and bridging toughness of short random fiber reinforced brittle matrix composites. *Journal of the Mechanics and Physics of Solids* 39(5): 607–625.

Lin Z, Kanda T and Li VC (1999) On interface property characterization and performance of fiber reinforced cementitious composites. *Concrete Science and Engineering* 1(3): 173–184.

Markovic I (2006) *High-performance hybrid-fiber concrete – Development and utilization*. PhD Thesis, Delft University of Technology, Netherland, pp.50–57.

Naaman AE, Namur GG, Alwan JM, et al. (1991) Fiber pullout and bond slip. 1: Analytical study. *Journal of Structural Engineering, ASCE* 117(9): 2769–2790.

Pallett P, Gorst N, Clark L, et al. (2002) Friction resistance in temporary works materials. *Concrete* 36(6): 12–15.

Piggott MR (1980) *Load Bearing Fibre Composites*. Oxford: Pergamon Press, p. 277.

Uchida Y, Niwa J, Tanaka Y, et al. (2005) Outlines of 'recommendations for design and construction of ultra high strength fiber reinforced concrete structures' by JSCE. In: *Proceedings of international RILEM workshop on high performance fiber reinforced cementitious composites in structural applications*. Honolulu, Hawaii: RILEM Publications SARL, 2006, pp.343–351.

Wille K and Naaman AE (2013) Effect of ultra-high-performance concrete on pullout behavior of high-strength brass-coated straight steel fibers. *ACI Materials Journal* 110(4): 451–462.

Wille K, Tue VT and Parra-Montesinos GJ (2014) Fiber distribution and orientation in UHP-FRC beams and their effect on backward analysis. *Materials Structure* 47(11): 1825–1838.

Yoo DY (2014) *Performance enhancement of ultra-high-performance fiber-reinforced concrete and model development for practical utilization*. PhD Thesis, Korea University, Seoul, Korea, p.586.

Yoo DY, Banthia N, Kim SW, et al. (2015a) Response of ultra-high-performance fiber-reinforced concrete beams with continuous steel reinforcement subjected to low-velocity impact loading. *Composite Structures* 126: 233–245.

Yoo DY, Kang ST, Lee JH, et al. (2013a) Effect of shrinkage reducing admixture on tensile and flexural behaviors of UHPFRC considering fiber distribution characteristics. *Cement and Concrete Research* 54: 180–190.

Yoo DY, Kang ST and Yoon YS (2014) Effect of fiber length and placement method on flexural behavior, tension-softening curve, and fiber distribution characteristics of of UHPFRC. *Construction and Building Materials* 64: 67–81.

Yoo DY, Kim J, Zi G, et al. (2015b) Effect of shrinkage-reducing admixture on biaxial flexural behavior of ultra-high-performance fiber-reinforced concrete. *Construction and Building Materials* 89: 67–75.

Yoo DY, Lee JH and Yoon YS (2013b) Effect of fiber content on mechanical and fracture properties of ultra high performance fiber reinforced cementitious composites. *Composite Structures* 106: 742–753.

Zhao Z, Kwon SH and Shah SP (2008) Effect of specimen size on fracture energy and softening curve of concrete: Part I. Experiments and fracture energy. *Cement and Concrete Research* 38(8): 1049–1060.

Notation

a, b empirical coefficients

A_f area of fiber, mm^2

A_m area of matrix ($A_m = 100 \times A_f$), mm^2

d_f diameter of fiber, mm

E_f elastic modulus of fiber, GPa

ε_m local strain of matrix

E_m elastic modulus of matrix, GPa

f_t first cracking tensile strength in composites, MPa

G_m shear modulus of matrix at interface $\left[G_m = \frac{E_m}{2 \times (1 + v_m)} \right]$, GPa

κ initial slope of bond stress versus slip relation

l embedment length of fiber, mm

l_f length of fiber, mm

N_b number of fiber in a unit area

$p(l)$ probability density function for embedment length

$p(\theta)$ probability density function for fiber orientation distribution

P pullout load, kN

P_{max} maximum pullout load, kN

P_{crit}, δ_{crit} critical pullout load and slip when partial debonding occurs, kN and mm

P_0, δ_0 pullout load and slip related to the frictional shear stress, kN and mm

r_f radius of fiber, mm

R_m radius of the matrix around the fiber, mm

u length of debonding zone, mm

V_f volume fraction of fiber

V_m volume fraction of matrix

w crack width, mm

w_s crack width when the fiber starts to slide at the interface, mm

x distance from the end of fiber, mm

α constant determining initial slope of frictional slip behavior

δ slip displacement, mm

δ_0 end slip of fiber at the onset of full debonding, mm

$\delta_{\text{utl.}}$ ultimate pullout slip, mm

ε_c strain in composites

η factor reflecting steepness of descending branch in fiber pullout curve

η_l length efficiency factor in the pre-cracking case for frictional stress transfer mechanism

η_θ fiber orientation coefficient

γ, n coefficients for β in equation (16)

μ frictional coefficient at the fiber-matrix interface

v_f Poisson's ratio of fiber

v_m Poisson's ratio of matrix

σ_b fiber-bridging stress, MPa

σ_c stress in composites, MPa

σ_f stress in fiber, MPa

σ_m stress in matrix, MPa

σ_{mt} tensile stress in matrix, MPa

σ_{ub} fiber-bridging strength, MPa

θ inclination angle of fiber with respect to the loading direction

τ local shear stress at interface between the fiber and the matrix, MPa

τ_f frictional shear strength, MPa

$\tau_{f(app)}$ apparent frictional shear strength, MPa

τ_{fd} decaying frictional shear stress, MPa

$\tau_{\max(app)}$ apparent bond strength, MPa

$$\lambda = \sqrt{KQ}$$
$$Q = 1 + \frac{A_m E_m}{A_f E_f}$$
$$K = \frac{\pi d_f \kappa}{A_m E_m}$$